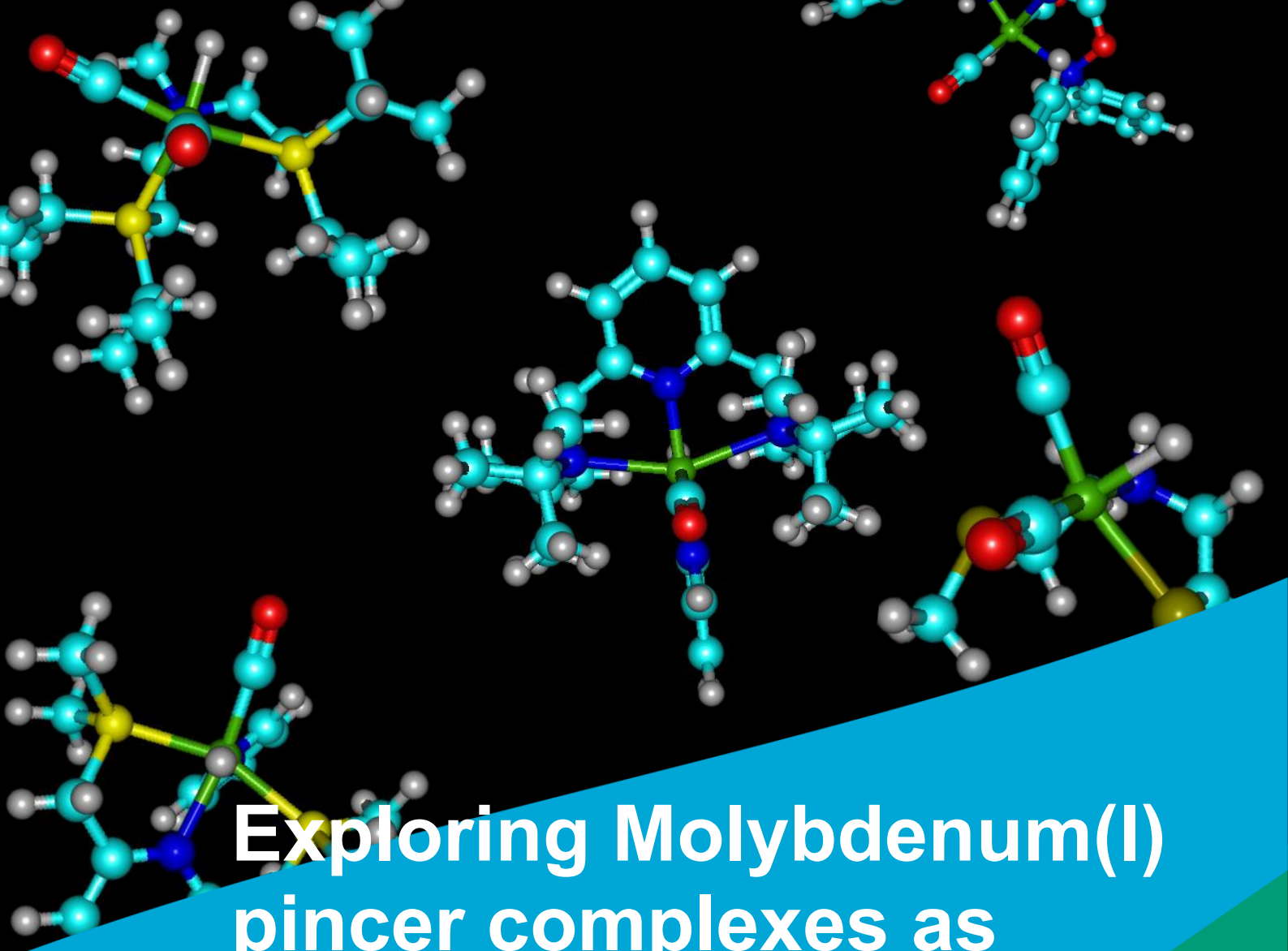

Exploring Molybdenum(I) pincer complexes as Catalysts for Pyridine Hydrogenation

Structure Prediction via MACE and Energetic Evaluation Using DFT

Author: O. Koele

Date: July 15, 2025

TU Delft

Exploring Molybdenum(I) pincer complexes as Catalysts for Pyridine Hydrogenation

By

Olaf Koele

to obtain the degree of Bachelor of Science
at the Delft University of Technology
to be defended publicly on Tuesday July 22, 2025 at 01:00 PM

Performed at:
Inorganic systems Engineering
Chemical Engineering
Faculty of Applied Sciences

Under supervision of:
Prof. Dr. E.A. Pidko
Dr. A.A. Kolganov
MSc A.V. Kalikadien

Student number:	5792681/s3555062	
Project duration:	April 24, 2025 – July 15, 2025	
Thesis committee:	Prof. Dr. E.A. Pidko,	TU Delft, supervisor
	Dr. T. Bouwens,	TU Delft

TU Delft

ISEgroup ChemE @ TU Delft

Abstract

As the transition to cleaner energy intensifies, N-heterocycles as liquid organic hydrogen carriers (LOHCs) offer a promising approach. However, their reliance on noble metals such as ruthenium, iridium, and platinum poses sustainability challenges.
In this study, 60 Mo(I) pincer complexes were screened using a combination of MACE and DFT. MACE was used to generate initial 3D molecular structures via force field optimization. These were further analysed using DFT calculations with the PBE0-D3BJ functional and def2-SVP basis set under standard conditions. Gibbs free energies were computed and used to evaluate pyridine binding energies across the ligand set.
The results indicate that pyridine binding to Mo(I) complexes is unfavourable, despite several complexes exhibiting sufficiently hydridic Mo-H bonds to suggest potential catalytic activity. The hydride charge appears to be conformation dependent, with certain configurations decreasing or increasing the hydridic charge. Oxidation of Mo(I) was observed in some systems, leading to pincer ligand decomposition. Additionally, nitrogen donor arms often dissociate from the metal centre, resulting in 5-coordinated geometries.
The unfavourable binding energy suggest that inner sphere mechanisms are unlikely. Instead, the findings support the plausibility of outer sphere pathways, especially given the lack of correlation between pyridine binding energy and the hydridic charge. Furthermore, the observed dissociation of nitrogen donor arms hint at potential ligand hemilability, which may influence catalytic dynamics and warrants further investigation.

Contents

1 Introduction

With the world transitioning towards cleaner energy, the demand for efficient hydrogen storage and utilization has surged. Placing hydrogen as a key vector for the green energy transition [1]. N-heterocycles, such as substituted pyridines, as liquid organic hydrogen carriers (LOHCs) offer a promising strategy. These compounds can reversibly store and release hydrogen through reversible hydrogenation and dehydrogenation, enabling safe and scalable hydrogen cycling [2]. While various derivatives have been explored, pyridine itself serves as a useful model. This is due to its low molecular weight and lack of inert substituents. The lower useless mass makes it more attractive for efficiency when compared to larger groups such as di-CH3pyridine. However, these processes are founded on noble metal catalysts, which are costly, scarce, and environmentally demanding. Discovery of efficient, earth-abundant alternatives is required to advance LOHC technologies [3].

Even if LOHCs offer a promising route for sustainable hydrogen storage, several issues remain. A key stap in LOHC cycling is hydrogenation, which typically occurs under harsh conditions and relies on noble metal catalysts. The best performing homogeneous hydrogenation catalysts are often organometallic coordination complexes. These complexes are based on noble metals such as ruthenium, iridium, and platinum. These have been widely explored and studied for their high activity and selectivity across a range of hydrogenation reactions. Including the reduction of ketones, alkenes and N-heterocycles [4], [5], [6]. However, these metals are scarce, expansive, and environmentally taxing. In contrast, base metals offer a more sustainable and cost-effective alternative. However, they tend to suffer from lower reactivity, reduced selectivity, and limited long-term stability. Molybdenum are particularly interesting due to its coordination chemistry and its role in redox-active enzymes [7]. However, molybdenum complexes have not yet been widely applied for (de)hydrogenation conversions. Only recently were there examples of Mo-catalysed hydrogenation. These include the hydrogenation of esters using bis(NHC) Mo complexes [8], the asymmetric hydrogenation of quinoline derivatives with a variety of Mo complexes [9], and the selective hydrogenation of amides catalysed by molybdenum pincer complexes [10]. This work focuses on the systematic screening of a series of Mo(I) pincer complexes as potential catalysts for the hydrogenation of pyridine. It aims to better understand the reactivity and assess their sustainability for LOHC related applications.

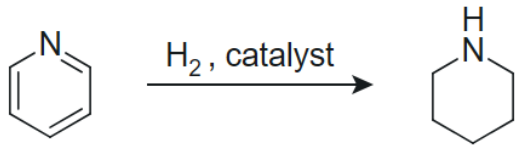

Figure 1.1: The hydrogenation of pyridine to piperidine.

There are limited design principles for the effective use of base-metal catalysts, despite the growing interest in them. While research into first-row metals like iron and cobalt has resulted in promising results for hydrogenation. However, issues with the functional groups tolerance and stability remain [11], [12]. In contrast to these systems, Molybdenum complexes have shown some success in hydrogenation. Mo(0) pincer complexes have shown catalytic activity in hydrogenation of amides [10]. However, studies into low-valent Mo(I) complexes are still rare. Furthermore, the amount of ligand backbones explored for Mo-based hydrogenation remains limited. This raises the question of how to

effectively evaluate and compare different ligand backbones in Mo(I) complexes in the pursuit to find a suitable catalyst for pyridine hydrogenation.

Recent advances in computational chemistry have created new possibilities for efficiently exploring the chemical space. Large scale simulations combined with systematic structure generation and statistical analysis allow for the fast evaluation of diverse ligand environments. Packages like MACE enable one to create initial 3D molecular models of transition metal complexes [13]. Offering a fast and flexible way of exploring different variations in metal ligand complexes. These models are valuable for studying transition metal complexes, including Mo(I), where minor changes in geometry can have significant effects on reactivity. Although such tools have been successfully applied to transition metal complexes such as Ru, Fe, Mn and Cu, their use with Mo(I) chemistry remains limited [13], [14]. This presents an opportunity to apply automated structure generation methods to explore the influence of systematic ligand variations, especially in the backbone or R-groups.

This project uses MACE to generate and explore Mo(I) complexes with a plethora of pincer ligand backbones. Every complex is examined in two versions: a complex with two carbonyl ligands and a complex where one of the carbonyl ligands is replaced by pyridine. Then geometry optimizations and energy calculations are done using density functional theory (DFT). Using the computed energies the substitution energy for carbonyl to pyridine is calculated. By varying the subgroups in every backbone ligand this project aims to explore trends in how ligands affect substitution energy. With the expanded goal of understanding steric features which promote favourable binding of pyridine. Which is a key step for designing an effective hydrogenation catalyst based on Mo(I) centres.

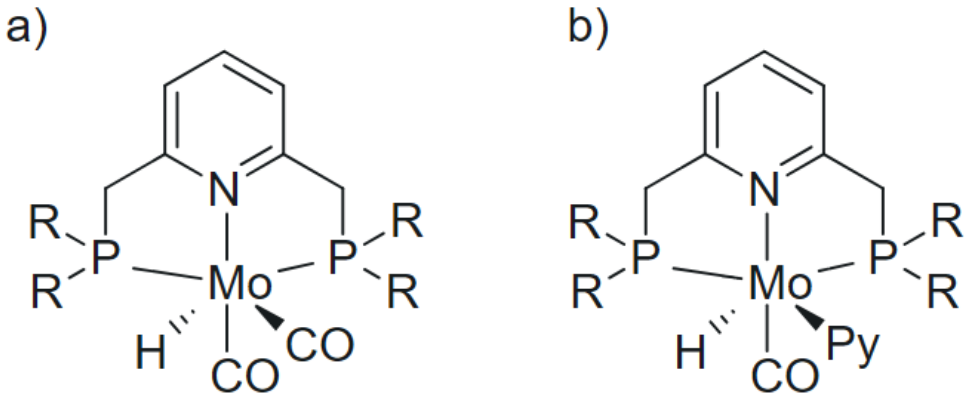

Figure 1.2: A schematic of a Molybdenum complex. These are the original complex (a), and with a pyridine (b) with PNP as pincer backbone.

2 Methods

This chapter describes the method and workflow used in this study. Section 2.1 describes the catalyst database and the methods to generate the complexes. Section 2.2 describes the methods behind the calculation. Section 2.3 describes the extraction and processing of data.

2.1 Catalyst Database

To evaluate the ligand effects on Mo(I) pincer complexes, a catalyst database was made. It contains eight different pincer ligand backbones with R- and X-group variations.

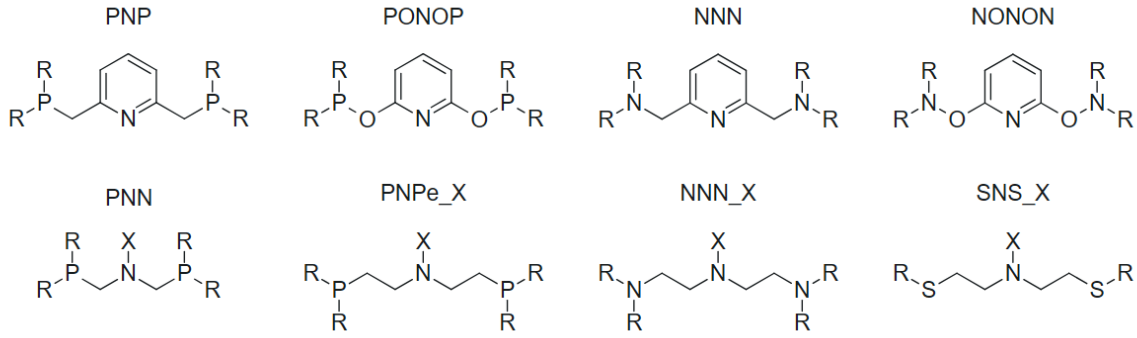

Figure 2.1: The eight ligand backbones of the database.

The substitutions depicted in Figure 2.1 are in the following table.

Table 2.1: substitution groups

X-groups	Me, H
R-groups	Me, iPr, tBu, Cy, Ph

Among the eight backbones, only four make use of the X-group. Together, including the substitution groups, there are 60 ligands in total.
As described in Figure 1.2, two variations of the complex were investigated. One structure containing the pincer ligand, a hydride, and two carbonyl groups, and another structure where one of the carbonyls was replaced with pyridine. Only the pyridine containing complexes were generated with MACE. The corresponding carbonyl complexes were obtained by replacing the pyridine ligand using a custom Python script applied to the copies of the original output files. This approach ensured consistent structural and naming formats across both sets of files, enabling direct, one-to-one comparison between the complexes. The pyridine complexes were chosen for generation in MACE because their coordination environment, comprising three distinct ligands (pyridine, carbonyl, and hydride), resulted in a greater number of conformers. Running MACE separately for both pyridine and carbonyl variants would have produced mismatched file counts due to the difference in conformer generation, as well as potential inconsistencies in automatic naming. This would have complicated the automated data matching and later binding energy calculations.

2.1.1 MACE

The initial 3D structures of the complexes were generated with the use of MetAl Complexes Embedding, in short MACE. MACE is a python-based tool designed for automated investigation of octahedral and square-planar structures and the generation of their atomic coordinates [13]. This software works particularly well for multidentate ligands, in my case those are the pincer ligands as seen in figure 2.1. It makes use of SMILES strings as a compact and text-based representation of the molecular structure of the ligands. SMILES represents the bond information in a linear format, which makes it useful for automated workflows. These SMILES are interpreted with the use of cheminformatic tools, such as RDKit to construct molecular graphs and allocates basic geometric data [15].
MACE applies force field theory (UFF) to the generated molecular graphs, which will result in an initial 3D structure. UFF approximates these geometries by minimizing the potential energy related to bond stretching, angle bending, out-of-plane bending, torsional, van der Waals and electrostatic interactions [16]. While UFF is not as accurate as quantum mechanical methods, it provides a reasonable starting point for refinement with density functional theory (DFT).

For the generation of the 3D structures of the pincer complexes, I started with constructing an Excel document. This document contains the defined catalyst database with SMILES strings for every variation. With each row of the document corresponds to a unique ligand backbone, which enables systematic parsing of the dataset.
Because the study involves octahedral complexes, the structure generation process is computationally intensive. MACE's performance particularly decreases when handling three distinct ligands, as is the case for the complexes containing hydride, carbonyl, and pyridine ligands. To improve efficiency, the workflow was modified to execute MACE in parallel across multiple logical processors, allowing for simultaneous runs. Additionally, the script was adapted to sequentially process the ligand variations from an Excel database. This setup enables a new ligand variation to begin immediately upon completion of a previous process. Which results in a significant reduction in total generation time and minimizing manual intervention.

2.2 Density Functional Theory

To analyse the complexes generated from MACE, DFT calculations were performed. These calculations were conducted using the ORCA 6.0 software on the Snellius supercomputer [17]. Accurate modelling of larger molecules and transition metal complexes is enabled using specific functionals within ORCA., which determine their electronic energy states. MACE generates .xyz files for its complexes. These files contain the Cartesian coordinates of UFF-optimized metal-ligand complexes, which are then used in the input files using the chosen functionals. To streamline the process, A custom script was used that made input files from the Cartesian coordinates of the .xyz files. Given that Mo(I) complexes generally adopt a low-spin configuration in doublet state (S=1/2), the DFT calculations were carried out with a neutral charge and a multiplicity of 2
Following the Kohn-Sham theory, the Unrestricted Kohn-Sham (UKS) functional is used. This functional causes that the alpha- and beta-spin electrons are treated separately. Which makes it more suitable for unpaired electrons. DFT further optimizes the structures by adjusting the atomic positions to find the lowest-energy geometry with the Opt functional. After the optimization, the Freq functional calculates vibrational frequencies to confirm the true minimum. Which leads to obtaining thermodynamic properties such as enthalpy, entropy, and Gibbs free energy.

Electronic structure calculations were carried out using the PBE0 hybrid functional. This functional provides a balanced combination of Hartree-Fock exchange, PBE exchange and PBE correlation, making it suitable for calculations of molecular properties [18], [19]. However, this functional tends to overlook the van der Waals interactions. To solve this problem, the D3BJ dispersion correction is added, which adds those van der Waals interactions [20], [21]. The def2-SVP basis set was applied to describe the orbitals and their interactions [22].
The electronic energies obtained from these calculations were used to estimate thermodynamic properties such as internal energy, enthalpy, and entropy. These lead to the calculation of the Gibbs free energy in the gas phase. These Gibbs free energies come from the optimized structures, excluding electronic entropy contributions. All calculations were performed under standard conditions, T = 298.15 K and P 1.0 atm.

2.3 Extraction and calculations

To analyse the thermodynamic stability of the CO- and pyridine-complexes, I made a Python script that extracts the Gibbs free energies from the ORCA output files. This script then matches the Gibbs free energies of the CO complex with its corresponding pyridine complex based on backbone and R-group identifiers is the name of the output files. For each backbone and R-group combination, the most stable CO complex was selected as the reference. This reference would be compared to the pyridine complexes with the same backbone and R-group, this is to ensure the atom and electron count would remain the same.
Using the reference, the pyridine binding energy was calculated for each pyridine complex with the following equation:

$$\Delta G_{binding} = G(Mo\ L_3\ H\ CO\ Py) + G(CO) - G(Mo\ L_3\ H\ CO\ CO) - G(Py) \quad (2.1)$$

Here, L_3 represents the pincer ligand. G(CO) and G(Py) are the gas-phase Gibbs free energies of free carbonyl and pyridine. These values were taken from prior ORCA calculations. Then the binding Gibbs free energy was converted from Hartree to kJ/mol by the script. Finally, all results were exported to an Excel sheet, making comparison, visualisation and plotting of trends across ligands more accessible. To gather more information about reactivity, the charge on the hydride of carbonyl complexes were manually put into the Excel file.

3 Results & Discussion

In this study, 60 different pincer ligands were explored. Each of these pincer ligands had either 3 or 6 conformations depending on the flexibility of their donor arms. In total 580 calculations were carried out. With every calculation giving an output file where data about the complex could be extracted from. All calculations yielded completed output files, except for both PNN backbones. The files from MACE for these backbones were too erratic for DFT analysis.

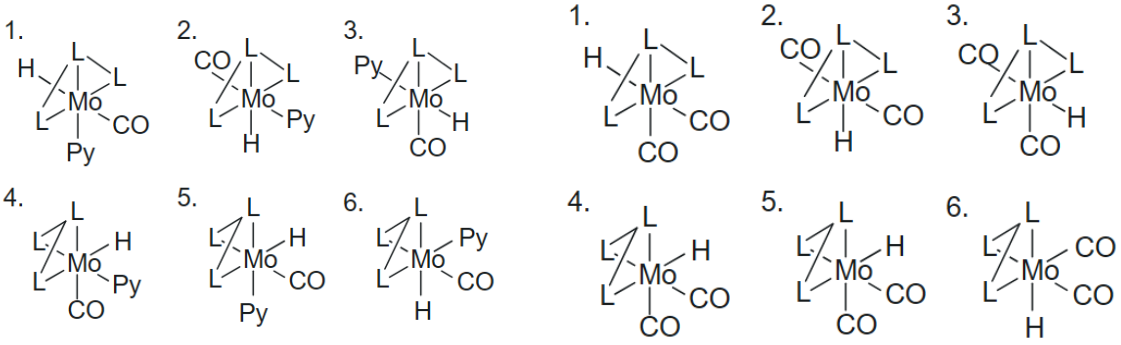

Figure 3.1: Different conformations of Mo-complexes with pyridine and carbonyl.

3.1 Reference States

To identify the most stable geometry per pincer, I calculated the relative Gibbs free energy of all conformers from the carbonyl complexes. This is done by comparing the lowest energy conformation with each conformation within the same backbone R-group combination as depicted in Figure 3.2. The lowest energy conformation is taken as reference state for later calculations. This reference state is also depicted on the bottom of Figure 3.2. These reference points allow for consistent comparisons of conformation stability.

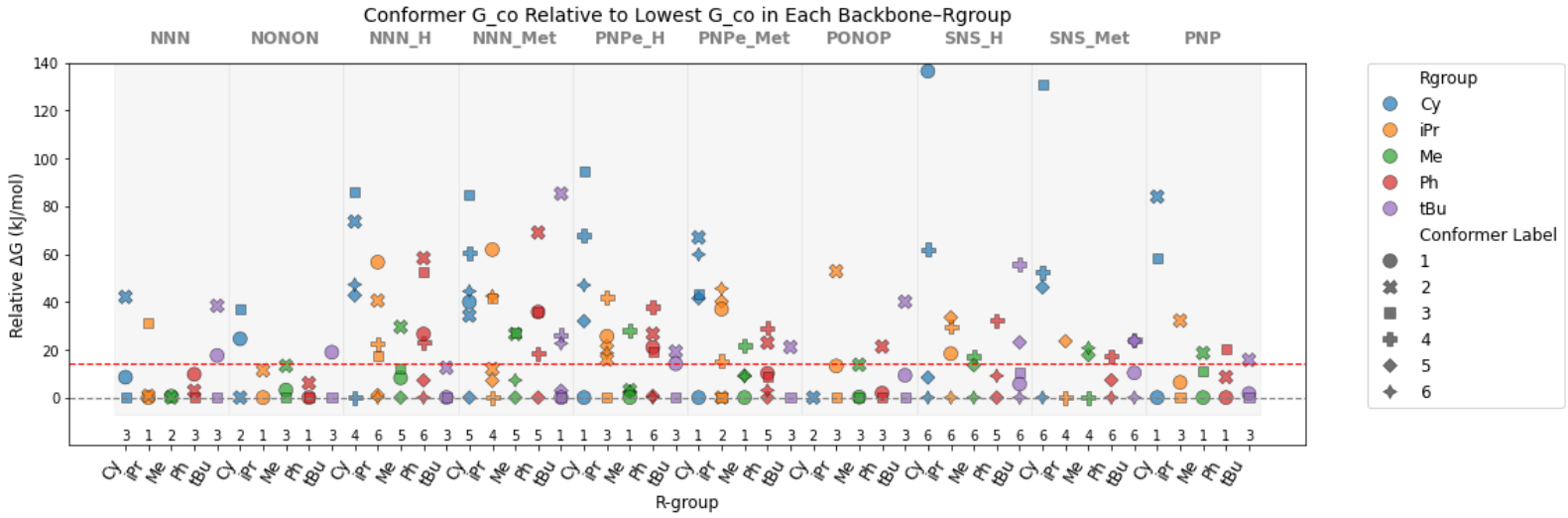

Figure 3.2: Graph depicting the relative ΔG between the reference and conformations. The reference conformation is stated below the datapoints. The red line depicts the cutoff point to where conformations are thermodynamically relevant under typical catalytic conditions.

In Figure 3.2 the zero-line represents the most stable conformation when compared to the other conformations in each backbone R-group combination. These most stable conformations are labelled at the bottom. Each data point has a different shape based on the conformer label; this is their conformation. The numbers of the conformer label represent the conformation as shown in Figure 3.1 Many of the configurations fall within a ΔG range of 0 to 50 kJ/mol. Though there are some outliers that exceed this range. Most of these outliers are found in the NNN and SNS backbones. NNN doubles this range to about 100 kJ/mol, while the SNS outliers almost triple it to about 140 kJ/mol. This suggests that certain conformations have a clear preference.
However, not all these conformations are catalytically relevant. At 100 °C (373.15 K), only conformations within approximately 14.3 kJ/mol of the most stable configuration would be populated at ≥1% at equilibrium. The configurations with higher ΔG values can be considered thermodynamically inaccessible under typical catalytic conditions. This is cutoff point is indicated as a red dotted line in Figure 3.2. As seen in Figure 3.2, there are few thermodynamically accessible configurations. Smaller R-groups have more thermodynamically accessible configurations, while larger R-groups have more thermodynamically inaccessible configurations. Ph is an exception, while being large, the group has a comparable amount of thermodynamically accessible configurations as Me over the different backbones.
The R-groups seem to affect the relative energy distribution spread in general. Systems with smaller R-groups such as methyl (Me) and isopropyl (iPr) show a lower variation of ΔG. While the larger R-groups such as phenyl (Ph) and cyclohexyl (Cy) show a much wider range of ΔG.

Overall configuration 3 (see Figure 3.1) seems to be the most favourable, with it being the reference state fifteen times as seen in Figure 3.3. Followed by configuration 1, with eleven counts, and configuration 6, with ten counts. Certain backbones show clear preference for conformations. PONOP for example has four counts for conformation 3, but only one count for conformation 2 as most stable conformer.
The backbones with elevated ΔG spread, SNS_X and NNN_X, show a clear preference for facial conformations (see Appendix E 1). For SNS_X, all reference states are facial, with a strong preference for conformation 6. There are in total seven counts for conformation 6, while the other facial conformation only has 3 counts. NNN_X also prefers the facial arrangements but has some meridional configurations as most stable conformer. The distribution of facial and meridional configurations for NNN_X is eight to two, with conformation 5 having four of the eight facial counts.
When there are multiple configurations that are close to each other, there is a preference to either configurations 1 or 3, it is rarely configuration 2 that is the most stable. Usually, the overlap only happens between configurations 1, 2 and 3. Whenever there are more than 3 configurations there is a clear preference between them.

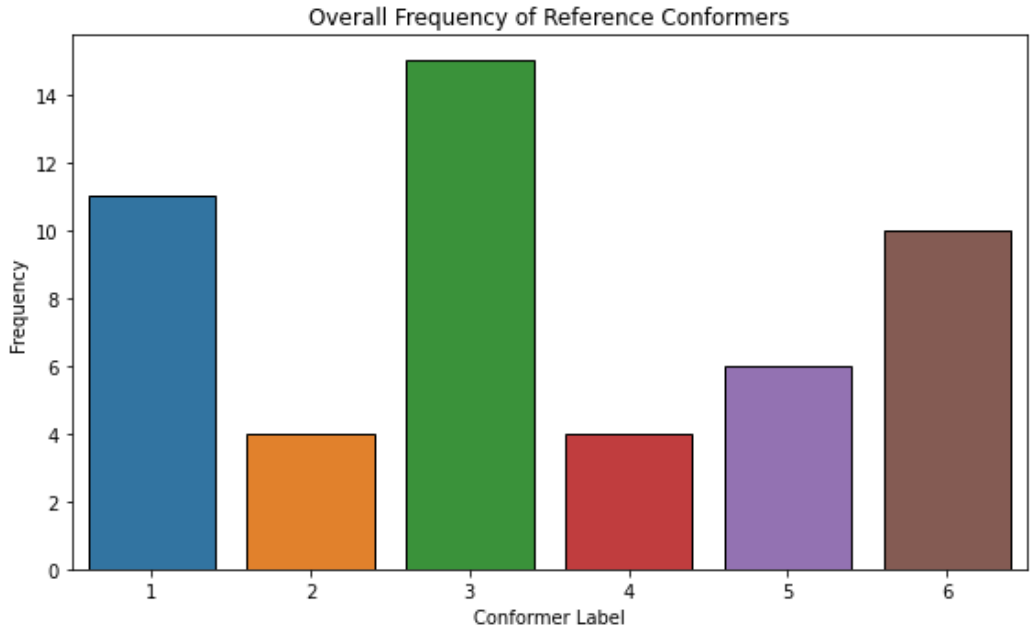

Figure 3.3: Graph depicting the frequency of most stable conformers in the carbonyl complexes.

3.2 Pyridine Binding Energy

To analyse the thermodynamic stability of the pyridine complexes, I graphed the pyridine binding energy. This binding energy was calculated with formula 2.1. The Gibbs free energies for the standalone pyridine and carbonyl are taken from prior ORCA calculations (see Appendix A for full numerical values). The results of formula 2.1 are plotted in Figure 3.4. For the Gibbs free energy of the CO-complex, the most stable conformation (reference state) within each backbone R-group combination was used, as shown in Figure 3.2.

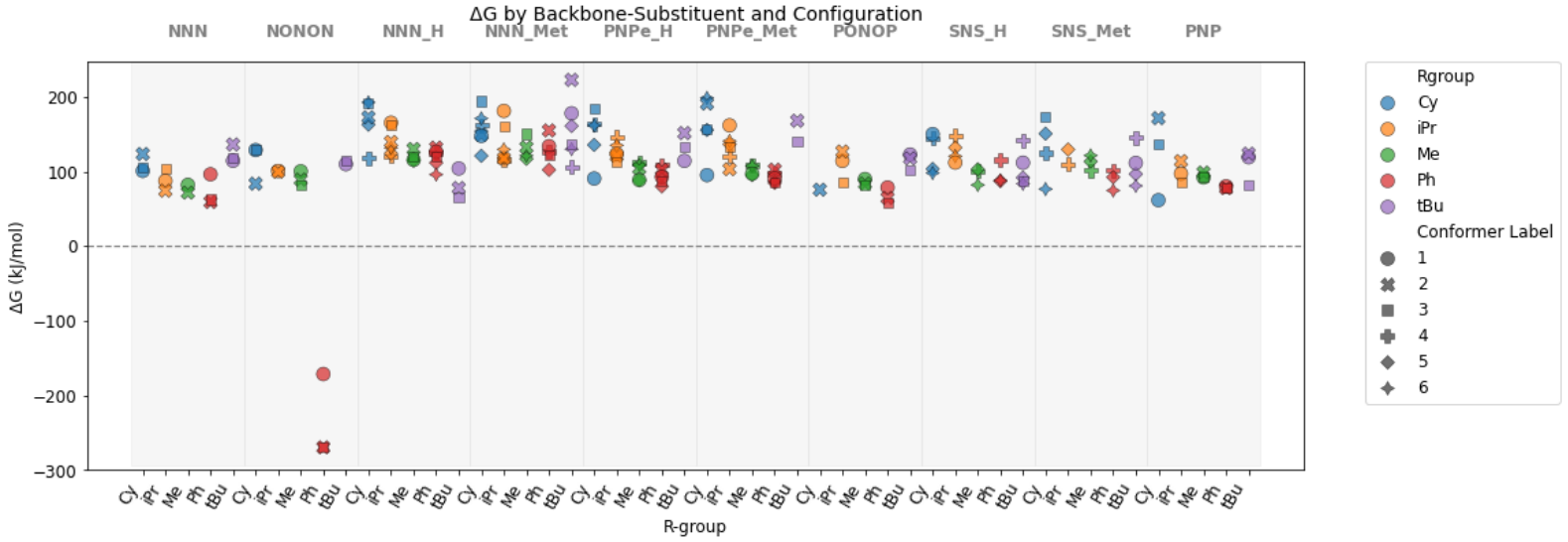

Figure 3.4: The pyridine substitution energy for every Backbone R-group combination.

The calculated Gibbs free energies for all backbone R-group combinations are generally highly positive, indicating that ligand substitution is unfavourable in most cases. This suggests that carbonyl complexes do not favour pyridine coordination. An exception for this trend is NONON-Ph, which shows a very negative ΔG. Indicating a thermodynamically favoured substitution. However, inspection of the optimized structures reveals that this is due to ligand decomposition rather than actual pyridine binding. As shown in Figure 3.5, the pincer backbone completely breaks apart in all three configurations. This decomposition is likely due to oxidation of molybdenum(I), which destabilizes the ligand framework.

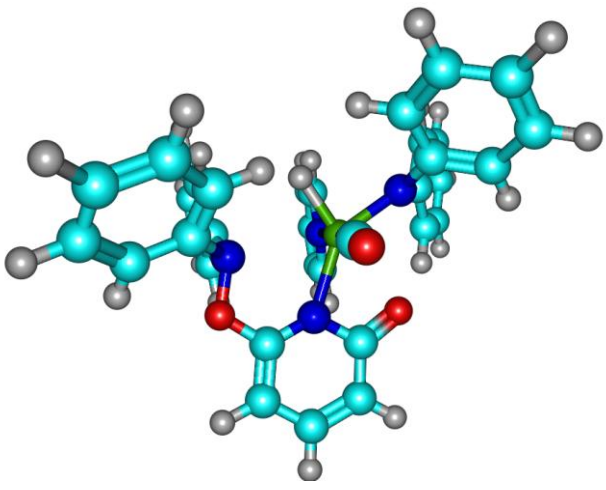

Figure 3.5: The optimized structure of NONON Ph meridional axial to H (configuration 2).

The spread of ΔG is influenced by substitution group size. Smaller R-groups like Me and iPr show a tight distribution. While the bulkier R-groups such as Cy and tBu show a broader spread. Despite being a large substituent, phenyl shows a narrower ΔG spread, which is more comparable to smaller R-groups. This was also observed in Figure 3.2. When examining the optimized structures, it reveals that this is due to phenomenon called π-stacking. Π-stacking is an attractive force between two aromatic rings, in this case Ph and pyridine, and stabilizes the structure [23]. Figure 3.6 shows the π-stacking in PNP-Ph meridional axial to CO (conformation 3) between two Ph groups and pyridine.

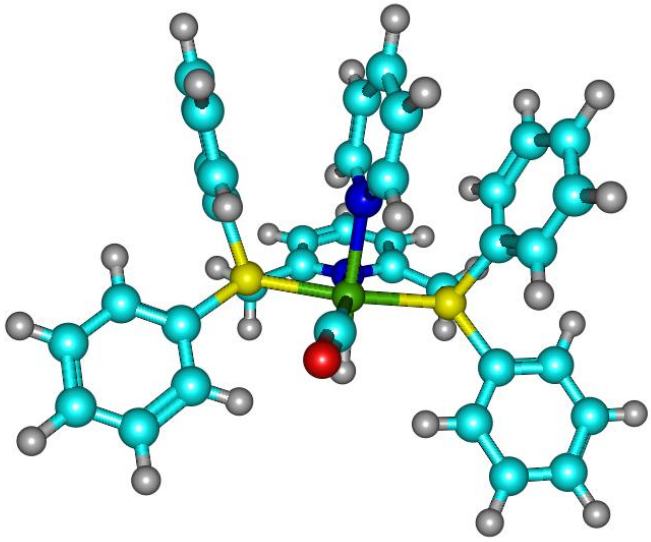

Figure 3.6: The optimized structure of PNP Ph meridional axial to CO (conformation 3).

In the dataset, systems featuring nitrogen arms tend to show a higher maximum ΔG value across configurations. These backbones show less favourable thermodynamics for carbonyl substitution. Examination of the optimized structures shows that nitrogen arms frequently dissociate from the metal centre, sometimes both arms dissociate. This results in 5-coordinated geometries, which destabilizes the complex and contributes to higher ΔG. This could indicate the possibility of hemilablity, however hemilability usually stabilises intermediates [24]. In this case the higher ΔG implies that the dissociated forms are likely not stabilizing. Examples of such dissociation can be found in Appendix D.

For sulphur-containing backbones (SNS_X), a different issue occurs. Here, the backbone would dissociate away from their sulphur arms resulting in broken pincer backbones (see Appendix D for examples). This only occurred in meridional configurations of the SNS structures. These meridional configurations were unable to be processed by ORCA. Of the meridional configurations, only configuration 1 could provide a complete structure when the R-group is tBu. This again indicates that molybdenum(I) can be oxidized and decomposes the pincer backbone of the metal complex. With meridional configurations being more rigid, it could that the structure flexibility has an influence on when Mo(I) oxidizes. However, the presence of tBu appears to inhibit the oxidation in certain conformers. This suggests that tert-butyl may provide steric protection stat prevents oxidation.

A comparison between different X-substituents on the pincer shows that the presence of methyl groups generally leads to higher ΔG values. This can be seen in the NNN_X pair as shown in figure

3.7. And similar patterns are visible in the SNS_X and PNPe_X backbones (see Appendix B). The increased ΔG values for Me groups indicates that the added steric bulk and electron donation disfavours the pyridine substitution.

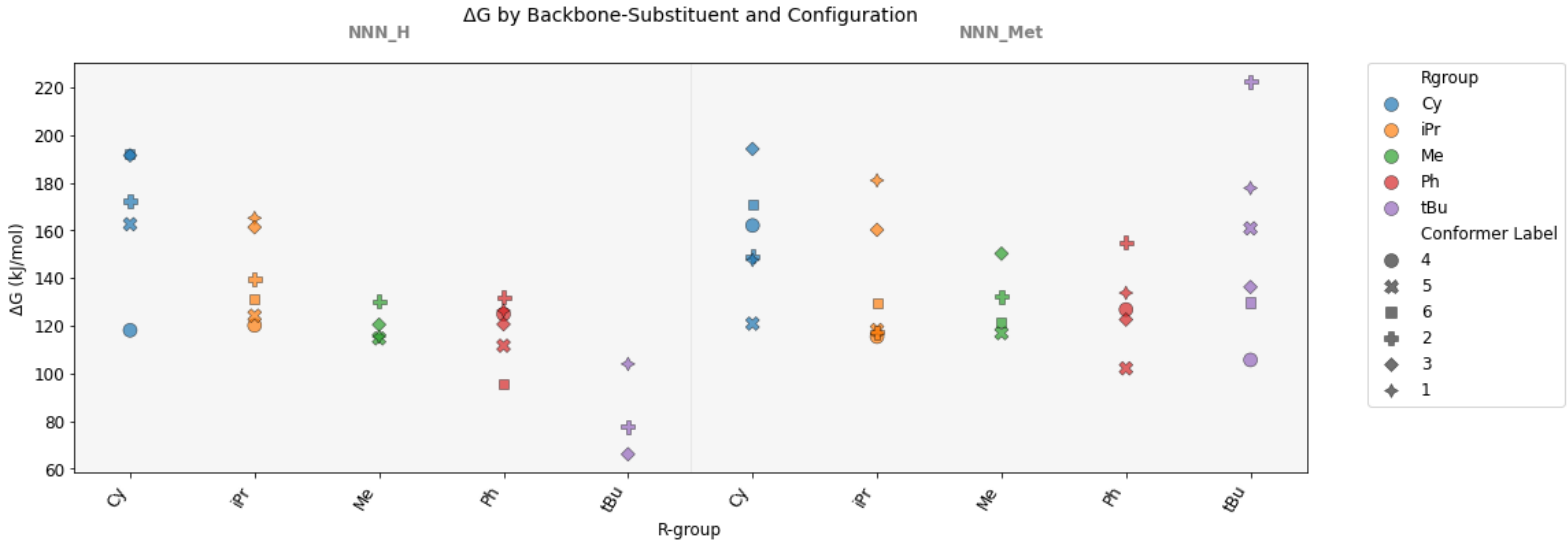

Figure 3.7: A graph depicting the substitution energies of NNN_Me and NNN_H.

To investigate how pyridine coordination changes the most stable configurations, the pyridine binding energies were plotted in the same format as Figure 3.2. Notably, pyridine coordination reduces the overall energetic spread between conformers (as seen in Figure 3.8). This indicates that binding pyridine makes systems more configurationally fluxional.

As seen in Figure 3.9, there is a more even distribution of most-stable conformations. Conformer 3 became less prevalent when compared to the carbonyl complexes, while conformers 2 and 5 became more prevalent. Individual backbones show the same preferences as in the carbonyl complexes. Configuration 3 has a lower preference, which contributes to an overall even distribution of most-stable conformers (See Appendix E 2). Again, indicating that pyridine coordination makes the system more configurationally fluxional.

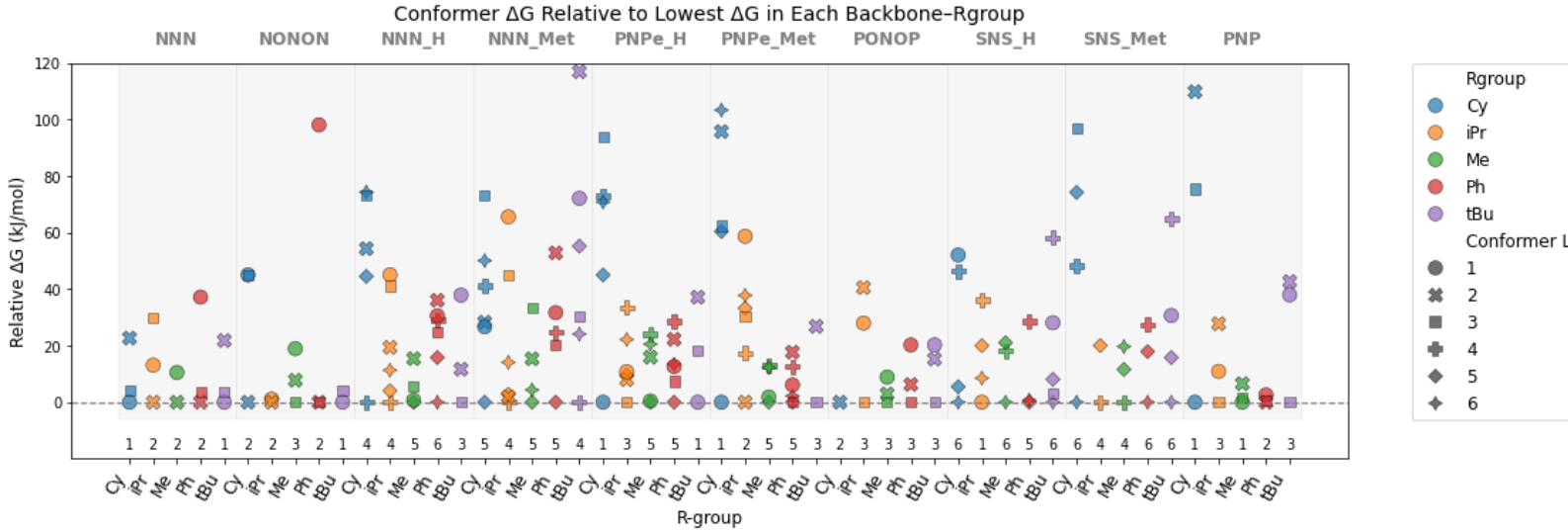

Figure 3.8: Graph depicting the relative ΔG between the most-stable conformer and other conformations in the same backbone substituent combination.

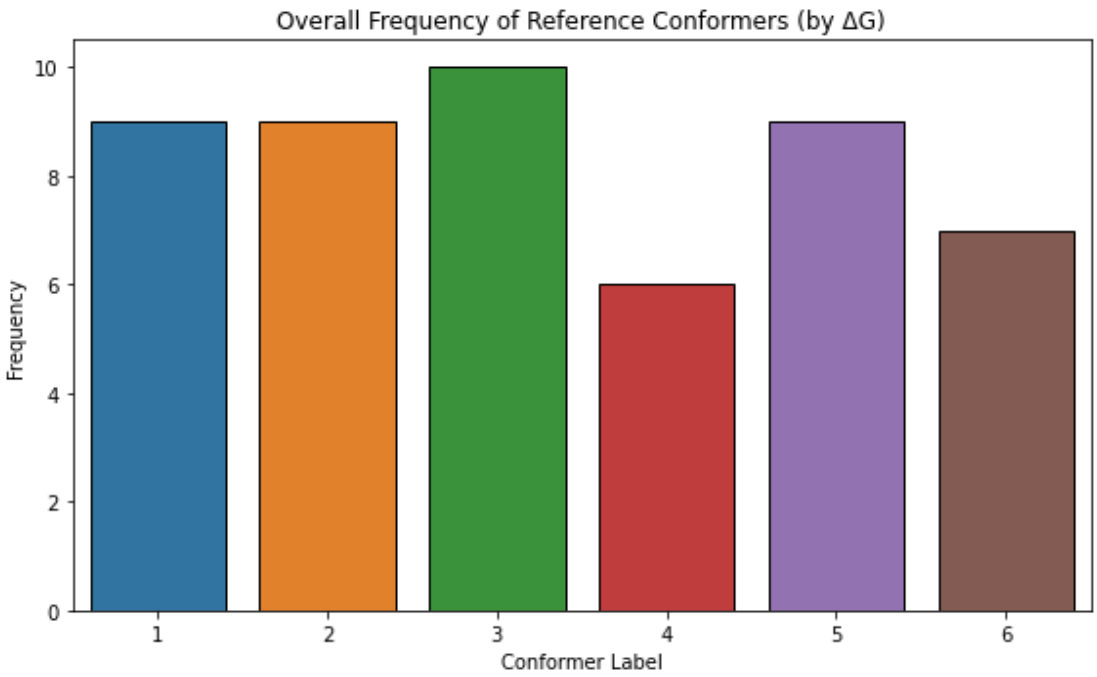

Figure 3.9: Graph depicting the frequency of most stable conformers in the pyridine complexes.

3.3 Hydride Partial Charge

To better understand the reactivity of the investigated complexes, the partial charge on the hydride ligand was examined. This charge would be as a proxy of reactivity, based on the assumption that negatively charged hydrides are more nucleophilic. And thus are more reactive in substitution or transfer processes [25]. Figure 3.10 plots the Gibbs free energy of pyridine substitution against the hydride charge of their carbonyl complexes.

While no clear correlation emerged between hydride charge and ΔG, several notable trends appear across different conformations and backbones. Most configurations fall within a hydride charge range of -0.10 to -0.20, with the facial structures (4, 5 and 6) only being found within this range. In contrast, conformation 2 is consistently less hydridic, clustering around -0.10 to 0, suggesting it is less reactive based on its hydride charge.

Configurations 1 and 3 span broader ranges. Configuration 1 varies from -0.25 to -0.05, while configuration 3 spans -0.30 to -0.10, making it the most hydridic on average. This is particularly interesting because configuration 3 is also the most frequently observed stable configurations across systems (see Figure 3.3). Implying a link between reactivity and geometric preference.

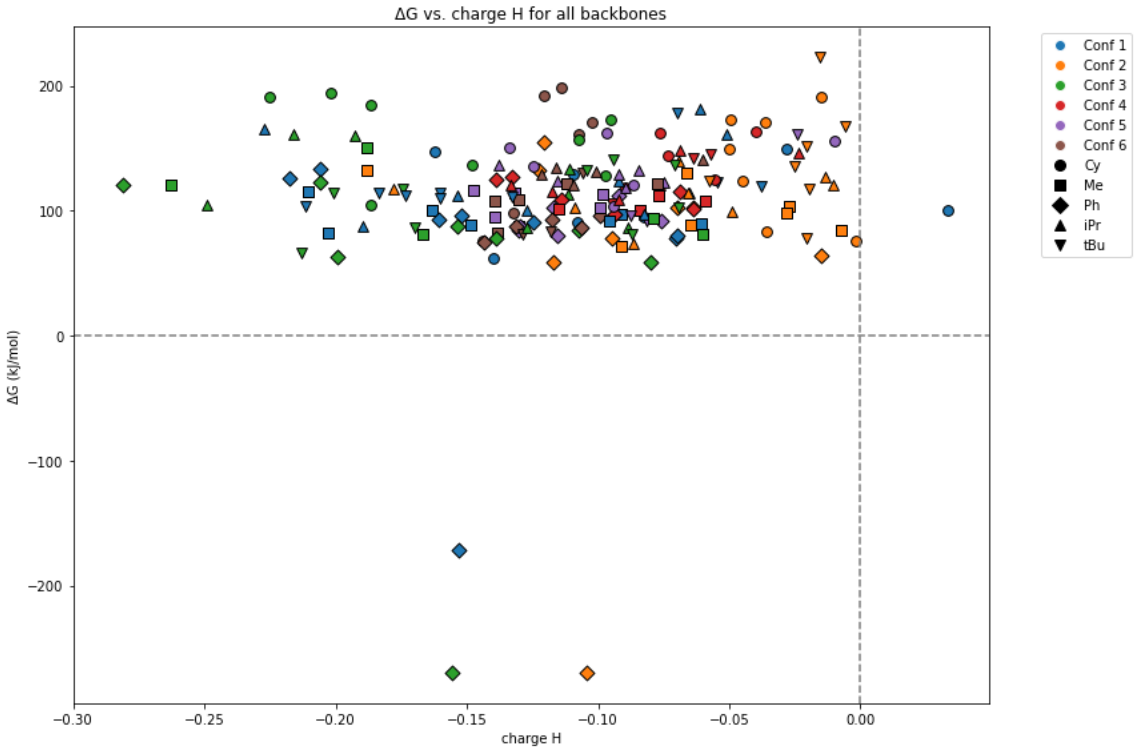

Figure 3.10: Graph comparing the substitution Gibbs free energy of pyridine against the charge on the hydride ligand.

These findings suggest that different configurations could be selectively stabilized to tune reactivity. The results indicates that configuration 3 leads to highly nucleophilic hydrides, while configuration 2 results in less reactive hydrides. Both these conformations can be stabilized by the right ligand choice. The data points to promising structure-reactivity relationships that could inform ligand design for the particular property of the hydride.

There are also outliers worth noting. The NONON-Ph is already found to be an outlier form the energy calculations, because of its ligand decomposition. Another outlier is the NNN-Cy configuration 1. It exhibits a positive charge. Upon inspection of its optimized structure, it shows that the hydride dissociates from the metal complex (see Figure 3.11).

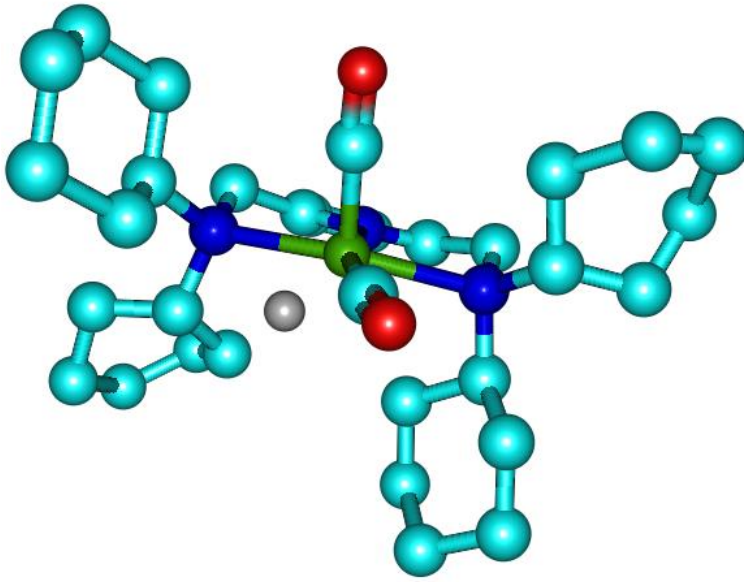

Figure 3.11: Optimized structure of NNN Cy meridional axial to pyridine (conformation 1). Here the hydrogens bonded to carbons are hidden for better overview of the dissociated H.

4 Conclusions and Outlook

This work focused on the systematic virtual screening of a series of Mo(I) pincer complexes as potential catalysts for the hydrogenation of pyridine. This work focused on the systematic virtual screening of a series Mo(I) pincer complexes as potential catalysts for the hydrogenation of pyridine. A library of pincer ligand backbones was created and used to generate 3D Mo(I) complexes with MACE. These structures were then optimized using DFT, which also provided thermodynamic properties. These properties were used to calculate pyridine binding energy.
The results suggest that Mo(I) pincer complexes are generally not suitable as catalysts for pyridine hydrogenation. Pyridine binding is unfavourable, and many conformations outside the most stable conformers are not catalytically relevant. However, the charge on hydrogen indicates some potential for reactivity. This charge can be influenced by conformations.
Structural trends show that bulky R-groups typically make pyridine binding more unfavourable. An exception are phenyl groups, which can engage in π-stacking interactions with the pyridine ligand. This effect results in binding energies comparable to systems with smaller substituents, like methyl. Additional trends were observed that impact pyridine binding. Nitrogen donor arms generally dissociate from the molybdenum metal centre. This results in less favourable pyridine binding in these systems. Furthermore, Mo(I) complexes can oxidize, which leads to decomposition of the pincer ligand backbone.

4.1.1 Implications

In general, if we assume for a catalyst to be active, it should firstly bind with pyridine and then still have a sufficiently hydridic Mo-H to proceed with the reaction. In the data there are systems with enough charge on the H for the system to be active. However, pyridine does not favourably bind to the complexes. This would mean that all these complexes are inactive and does not support inner sphere mechanisms. Outer sphere mechanisms are more likely, particularly given the lack of correlation between reactivity and pyridine binding. Further, the fact that nitrogen arms dissociate from the metal centre points to the possibility of ligand hemilability in Mo(I) complexes.

4.1.2 Limitations

A key limitation lies in the fact that molybdenum can oxidize and in turn can decompose any pincer ligand. This is demonstrated in the NONON Ph conformers but also in the SNS backbone. The study did not include any solvent effect or free energy corrections including entropy loss due to binding. The entropy loss is only implicitly included and does not explicitly model non-ideal entropy effect. The entropy changes in solution or condensed phase can be significantly different from the ideal gas approximation that ORCA uses by default.

4.1.3 Future Directions

Future studies of molybdenum(I) complexes should focus on the hemilability of the pincer donors. This is done to determine the feasibility of donor arm dissociation and recoordination. The five-coordinated structures of NNN_X suggest that there is a possibility that are five-coordinated intermediates in the reaction. Another future direction would be to explicitly assess whether ligand dissociation happens during the reaction, to see if the five-coordinate hypothesis holds true.
Multiple factors in this study suggest that inner sphere catalyst mechanisms are not possible with Mo(I) pincer complexes. Outer sphere mechanisms however are still a possibility. Given the lack of

favourable pyridine binding in this system but having hydridic systems would suggest that research into outer spere mechanisms would be an interesting next step.
Another interesting next step would be to research if there is any logic behind the oxidization of Molybdenum pincer complexes. From the data in this study, it seems that the rigidness of certain configurations has an influence on when Molybdenum oxidizes. It is also interesting to find out how tBu influences this oxidization process. In the SNS backbones it could counteract the oxidization process in certain configurations.

Bibliography

[1] K. Gomonov, C. T. Permana, and C. T. Handoko, ‘The growing demand for hydrogen: current trends, sectoral analysis, and future projections’, *Unconv. Resour.*, vol. 6, p. 100176, Apr. 2025, doi: 10.1016/j.uncres.2025.100176.

[2] P. Sánchez *et al.*, ‘Hydrogenation/dehydrogenation of N-heterocycles catalyzed by ruthenium complexes based on multimodal proton-responsive CNN(H) pincer ligands’, *Dalton Trans.*, vol. 49, no. 28, pp. 9583–9587, Jul. 2020, doi: 10.1039/D0DT02326D.

[3] S. Ramadhani *et al.*, ‘Advances in Catalytic Hydrogenation of Liquid Organic Hydrogen Carriers (LOHCs) Using High-Purity and Low-Purity Hydrogen’, *ChemCatChem*, vol. 16, no. 24, p. e202401278, 2024, doi: 10.1002/cctc.202401278.

[4] J. Ito, S. Ujiie, and H. Nishiyama, ‘New Bis(oxazolinyl)phenyl−Ruthenium(II) Complexes and Their Catalytic Activity for Enantioselective Hydrogenation and Transfer Hydrogenation of Ketones’, *Organometallics*, vol. 28, no. 2, pp. 630–638, Jan. 2009, doi: 10.1021/om800953f.

[5] M. V. Jiménez *et al.*, ‘Iridium(I) Complexes with Hemilabile N-Heterocyclic Carbenes: Efficient and Versatile Transfer Hydrogenation Catalysts’, *Organometallics*, vol. 30, no. 20, pp. 5493–5508, Oct. 2011, doi: 10.1021/om200747k.

[6] G. F. Santori, M. L. Casella, and O. A. Ferretti, ‘Hydrogenation of carbonyl compounds using tin-modified platinum-based catalysts prepared via surface organometallic chemistry on metals (SOMC/M)’, *J. Mol. Catal. Chem.*, vol. 186, no. 1, pp. 223–239, Jul. 2002, doi: 10.1016/S1381-1169(02)00188-7.

[7] J. P. Adamus, A. Ruszczyńska, and A. Wyczałkowska-Tomasik, ‘Molybdenum’s Role as an Essential Element in Enzymes Catabolizing Redox Reactions: A Review’, *Biomolecules*, vol. 14, no. 7, p. 869, Jul. 2024, doi: 10.3390/biom14070869.

[8] N. F. Both, J. Thaens, A. Spannenberg, H. Jiao, K. Junge, and M. Beller, ‘Hydrogenation of Esters Catalyzed by Bis(N-Heterocyclic Carbene) Molybdenum Complexes’, *ACS Catal.*, vol. 14, no. 6, pp. 4082–4092, Mar. 2024, doi: 10.1021/acscatal.4c00019.

[9] P. Viereck, G. Hierlmeier, P. Tosatti, T. P. Pabst, K. Puentener, and P. J. Chirik, ‘Molybdenum-Catalyzed Asymmetric Hydrogenation of Fused Arenes and Heteroarenes’, *J. Am. Chem. Soc.*, vol. 144, no. 25, pp. 11203–11214, Jun. 2022, doi: 10.1021/jacs.2c02007.

[10] T. Leischner, L. A. Suarez, A. Spannenberg, K. Junge, A. Nova, and M. Beller, ‘Highly selective hydrogenation of amides catalysed by a molybdenum pincer complex: scope and mechanism’, *Chem. Sci.*, vol. 10, no. 45, pp. 10566–10576, Nov. 2019, doi: 10.1039/C9SC03453F.

[11] S. Budagumpi *et al.*, ‘Progress in the catalytic applications of cobalt N–heterocyclic carbene complexes: Emphasis on their synthesis, structure and mechanism’, *Mol. Catal.*, vol. 535, p. 112850, Jan. 2023, doi: 10.1016/j.mcat.2022.112850.

[12] B. Sawatlon and P. Surawatanawong, ‘Mechanisms for dehydrogenation and hydrogenation of N-heterocycles using PNP-pincer-supported iron catalysts: a density functional study’, *Dalton Trans.*, vol. 45, no. 38, pp. 14965–14978, Sep. 2016, doi: 10.1039/C6DT02431A.

[13] I. Yu. Chernyshov and E. A. Pidko, ‘MACE: Automated Assessment of Stereochemistry of Transition Metal Complexes and Its Applications in Computational Catalysis’, *J. Chem. Theory Comput.*, vol. 20, no. 5, pp. 2313–2320, Mar. 2024, doi: 10.1021/acs.jctc.3c01313.

[14] S. Jeschke, K. Wilson, and A. F. Lee, ‘Accelerating Computational Modeling of Reactant Adsorption through a Combined MACE+DFT Approach: Furfural on Cu Surfaces’, *J. Phys. Chem. C*, Jun. 2025, doi: 10.1021/acs.jpcc.5c01790.

[15] A. V. Kalikadien, A. Mirza, A. N. Hossaini, A. Sreenithya, and E. A. Pidko, ‘Paving the road towards automated homogeneous catalyst design’, *ChemPlusChem*, vol. 89, no. 7, p. e202300702, 2024, doi: 10.1002/cplu.202300702.

[16] P. Tosco, N. Stiefl, and G. Landrum, ‘Bringing the MMFF force field to the RDKit: implementation and validation’, *J. Cheminformatics*, vol. 6, no. 1, p. 37, Jul. 2014, doi: 10.1186/s13321-014-0037-3.

[17] F. Neese, ‘The ORCA program system’, *WIREs Comput. Mol. Sci.*, vol. 2, no. 1, pp. 73–78, 2012, doi: 10.1002/wcms.81.
[18] C. Adamo, M. Cossi, and V. Barone, ‘An accurate density functional method for the study of magnetic properties: the PBE0 model’, *J. Mol. Struct. THEOCHEM*, vol. 493, no. 1, pp. 145–157, Dec. 1999, doi: 10.1016/S0166-1280(99)00235-3.
[19] C. Adamo and V. Barone, ‘Toward reliable density functional methods without adjustable parameters: The PBE0 model’, *J. Chem. Phys.*, vol. 110, no. 13, pp. 6158–6170, Apr. 1999, doi: 10.1063/1.478522.
[20] M. Stöhr, T. V. Voorhis, and A. Tkatchenko, ‘Theory and practice of modeling van der Waals interactions in electronic-structure calculations’, *Chem. Soc. Rev.*, vol. 48, no. 15, pp. 4118–4154, Jul. 2019, doi: 10.1039/C9CS00060G.
[21] S. Tsuzuki and T. Uchimaru, ‘Accuracy of intermolecular interaction energies, particularly those of hetero-atom containing molecules obtained by DFT calculations with Grimme’s D2, D3 and D3BJ dispersion corrections’, *Phys. Chem. Chem. Phys.*, vol. 22, no. 39, pp. 22508–22519, Oct. 2020, doi: 10.1039/D0CP03679J.
[22] ‘2.7. Basis Sets — ORCA 6.1 Manual’. Accessed: Jul. 12, 2025. [Online]. Available: https://orca-manual.mpi-muelheim.mpg.de/contents/essentialelements/basisset.html
[23] D. P. Malenov and S. D. Zarić, ‘Stacking interactions of aromatic ligands in transition metal complexes’, *Coord. Chem. Rev.*, vol. 419, p. 213338, Sep. 2020, doi: 10.1016/j.ccr.2020.213338.
[24] G. M. Adams and A. S. Weller, ‘POP-type ligands: Variable coordination and hemilabile behaviour’, *Coord. Chem. Rev.*, vol. 355, pp. 150–172, Jan. 2018, doi: 10.1016/j.ccr.2017.08.004.
[25] R. E. Adams, T. A. Grusenmeyer, A. L. Griffith, and R. H. Schmehl, ‘Transition metal hydride complexes as mechanistic models for proton reduction catalysis’, *Coord. Chem. Rev.*, vol. 362, pp. 44–53, May 2018, doi: 10.1016/j.ccr.2018.02.014.

Appendix A: full values of data

Full calculated energy value of pyridine: -247.75677837 Eh
Full calculated energy value of carbonyl: -113.11042514 Eh

Appendix B: Comparison graphs

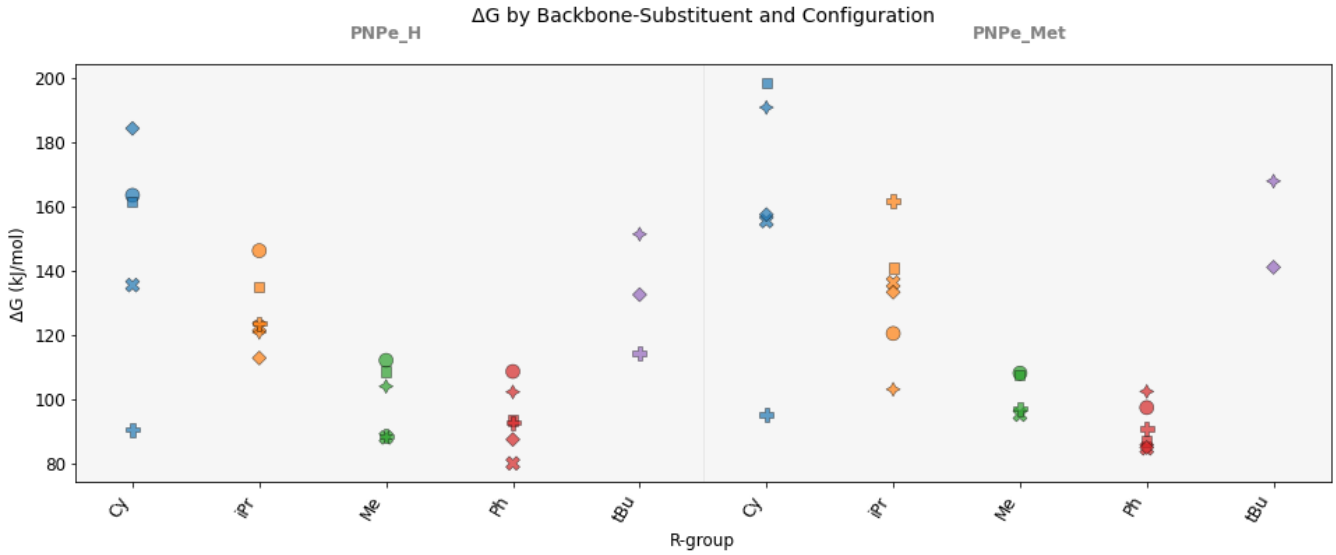

Appendix B 2: A graph of the substitution energies of PNPe_Me and PNPe_H

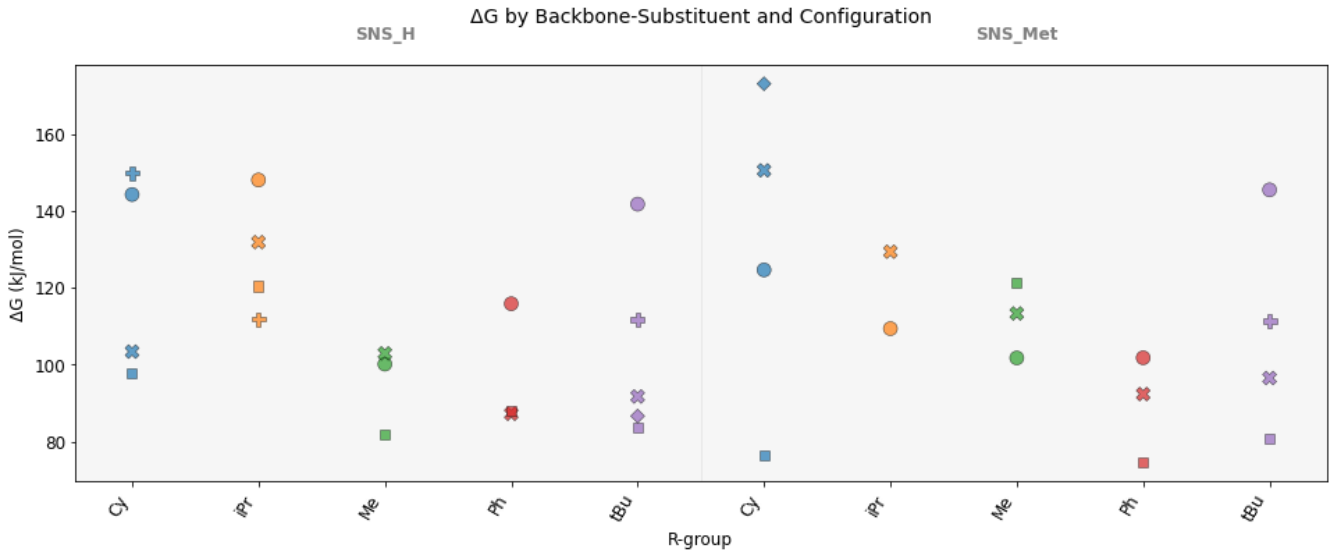

Appendix B 1: A graph of the substitution energies of SNS_Me and SNS_H

Appendix C: Hydride charges of Backbones

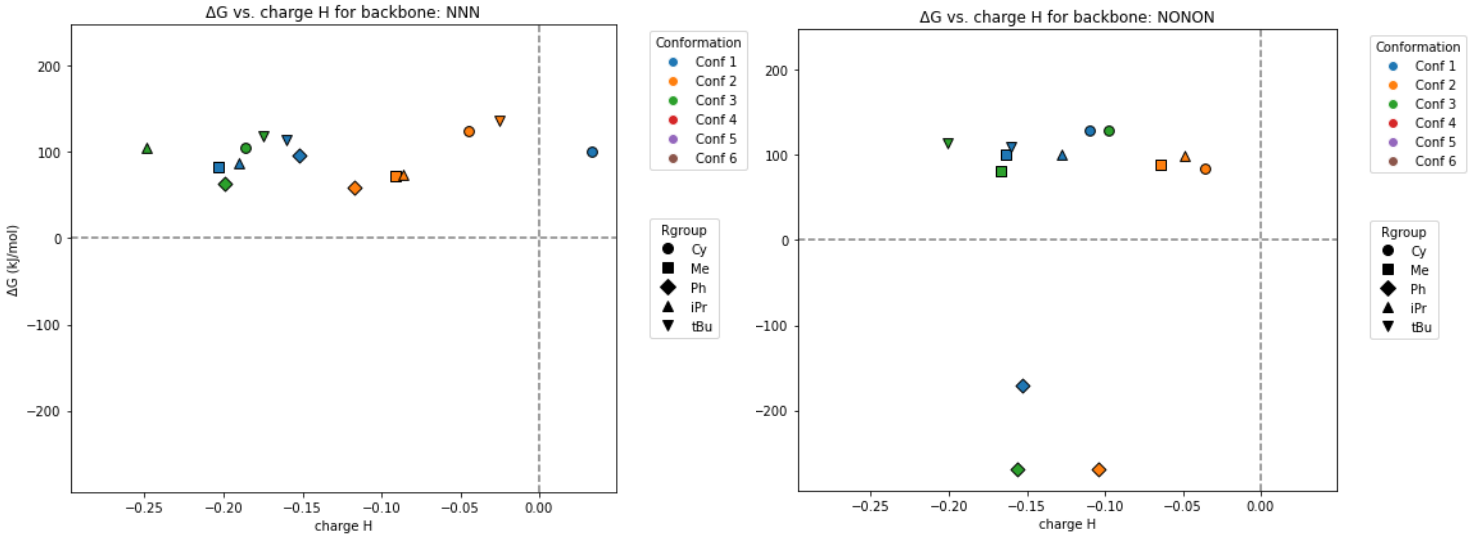

Appendix C 1: Graphs depicting the comparison between pyridine binding energy and the charge on the hydride bonded to Mo of NNN and NONON

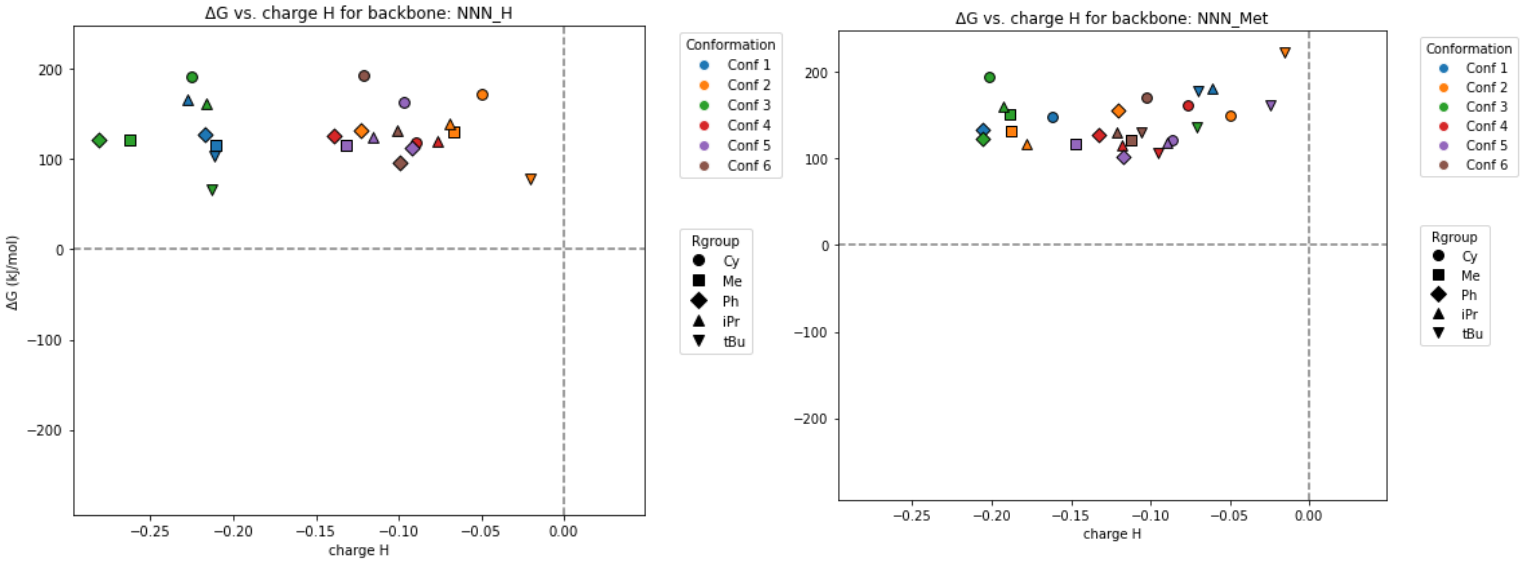

Appendix C 2: Graphs depicting the comparison between pyridine binding energy and the charge on the hydride bonded to Mo of NNN_H and NNN_Me

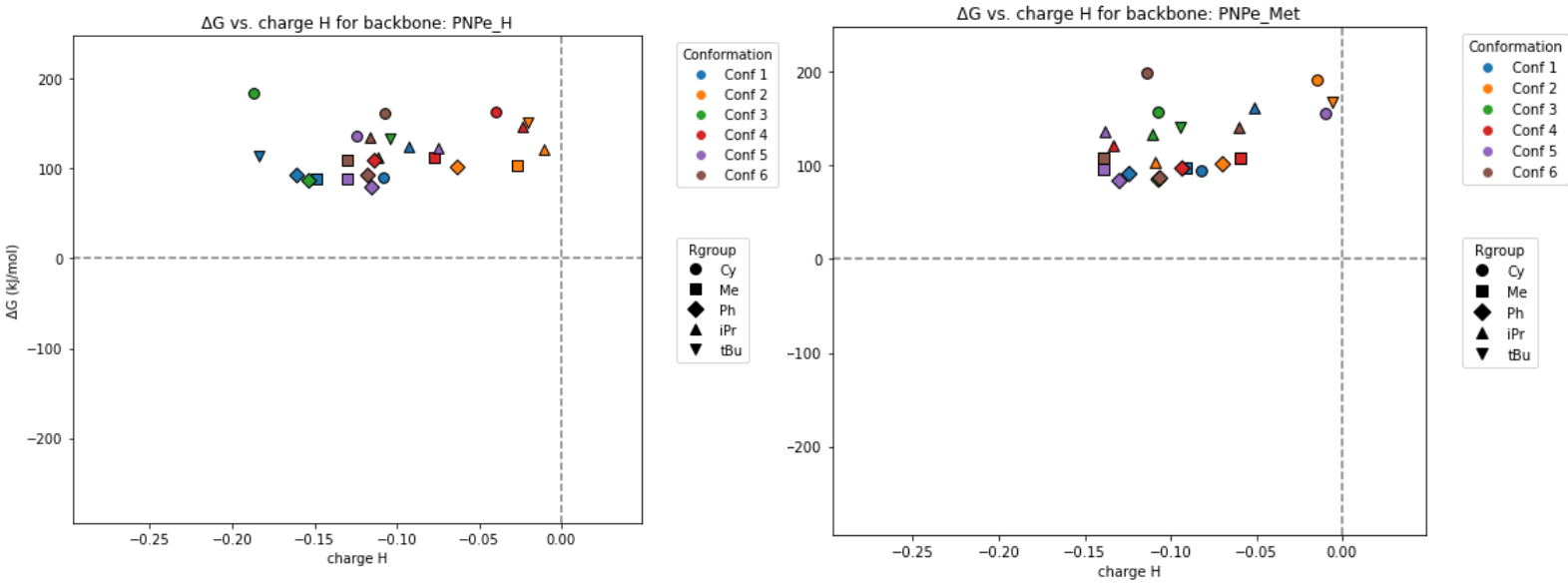

Appendix C 3: Graphs depicting the comparison between pyridine binding energy and the charge on the hydride bonded to Mo of PNPe_H and PNPe_Me

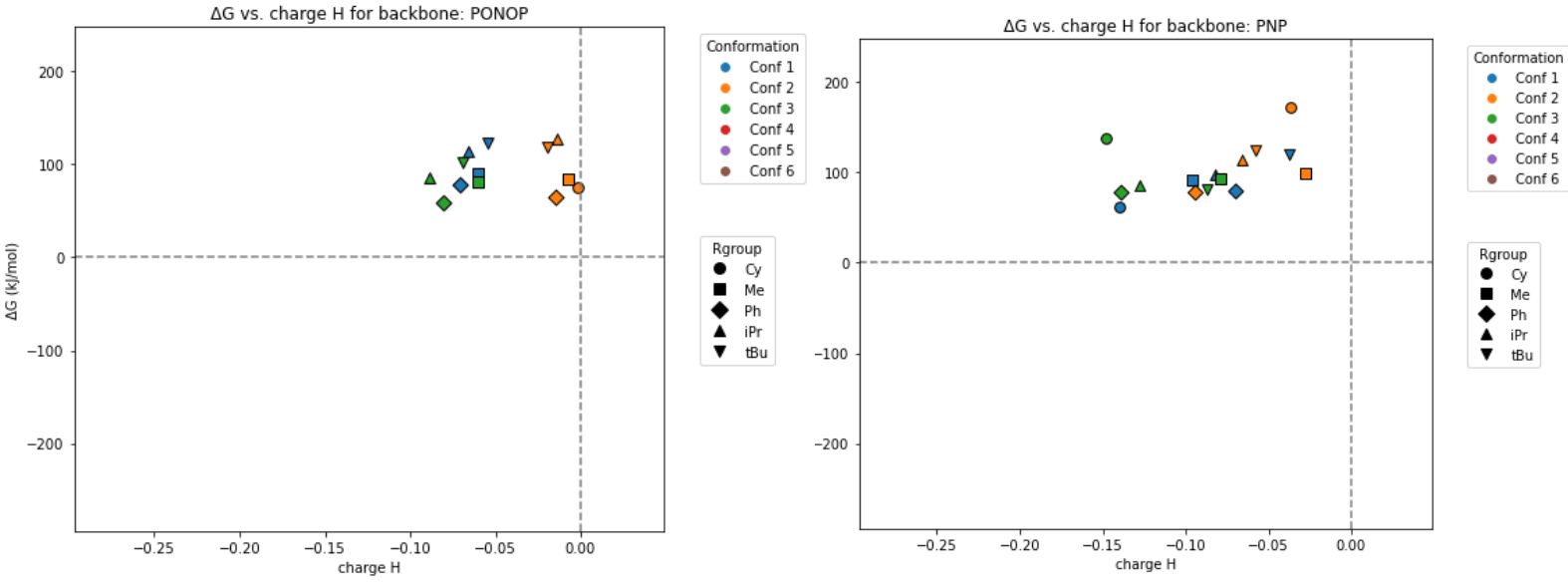

Appendix C 4: Graphs depicting the comparison between pyridine binding energy and the charge on the hydride bonded to Mo of PONOP and PNP

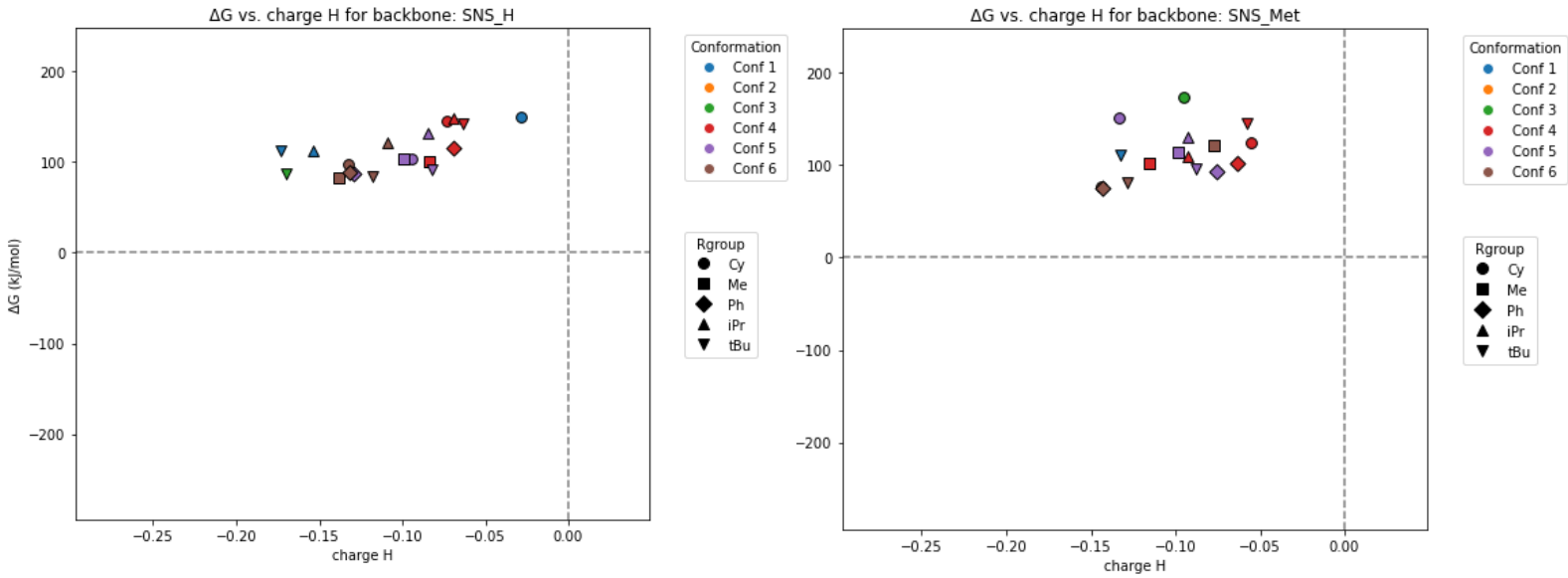

Appendix C 5: Graphs depicting the comparison between pyridine binding energy and the charge on the hydride bonded to Mo of SNS_H and SNS_Me

Appendix D: Optimized Structures

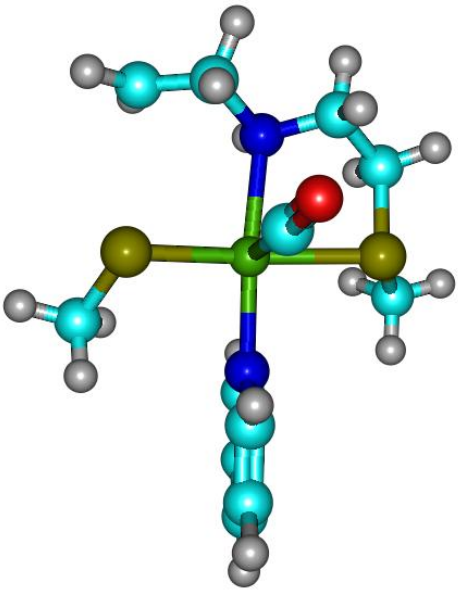

Appendix D 1: Optimized structure of SNS_H Me meridional axial to Py (conformer 1).

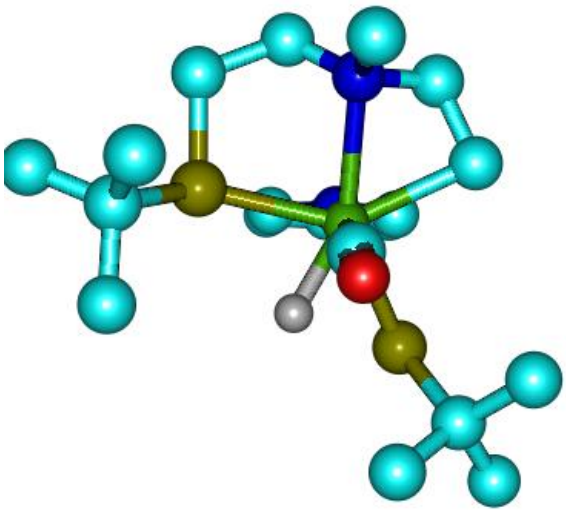

Appendix D 2: Optimized structure of SNS_Me tBu meridional axial to H (conformer 2). The H atoms bonded to carbon are hidden for visual clarity.

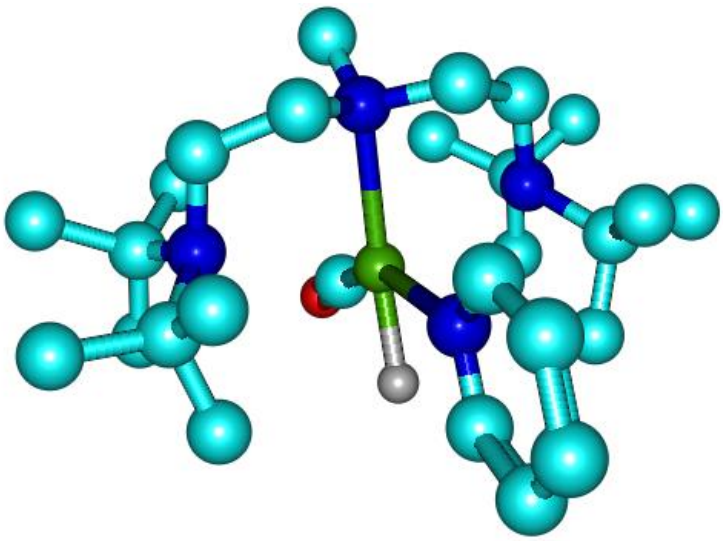

Appendix D 3: Optimized structure of NNN_Me tBu meridional axial to H (conformer 1). The H atoms bonded to carbon are hidden for visual clarity.

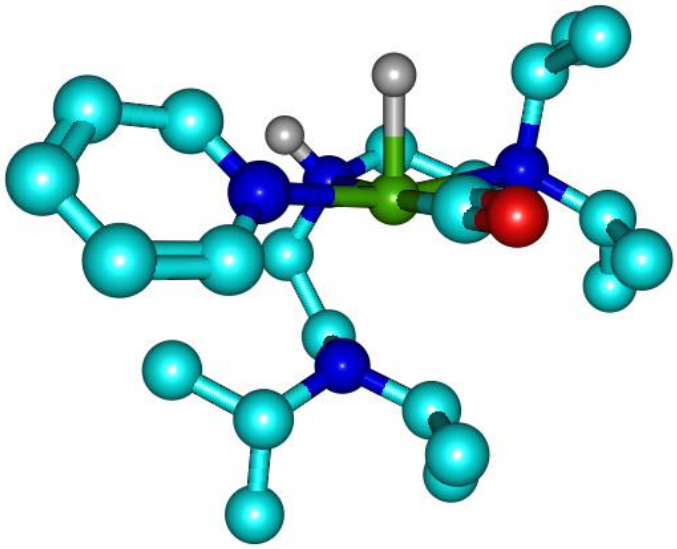

Appendix D 4: Optimized structure of NNN_H iPr facial axial to CO (conformer 4). The H bonded to carbon are hidden for visual clarity.

Appendix E: Reference conformers per Backbone

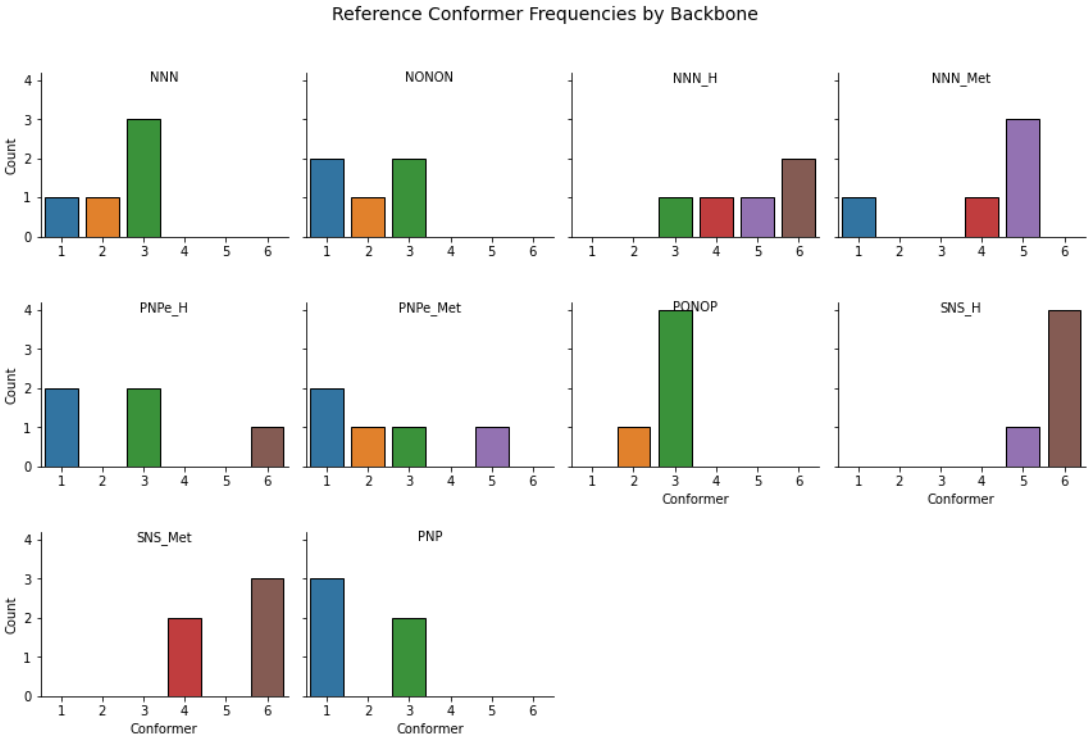

Appendix E 1: Graph depicting the frequency of most stable conformers per backbone for the carbonyl complexes

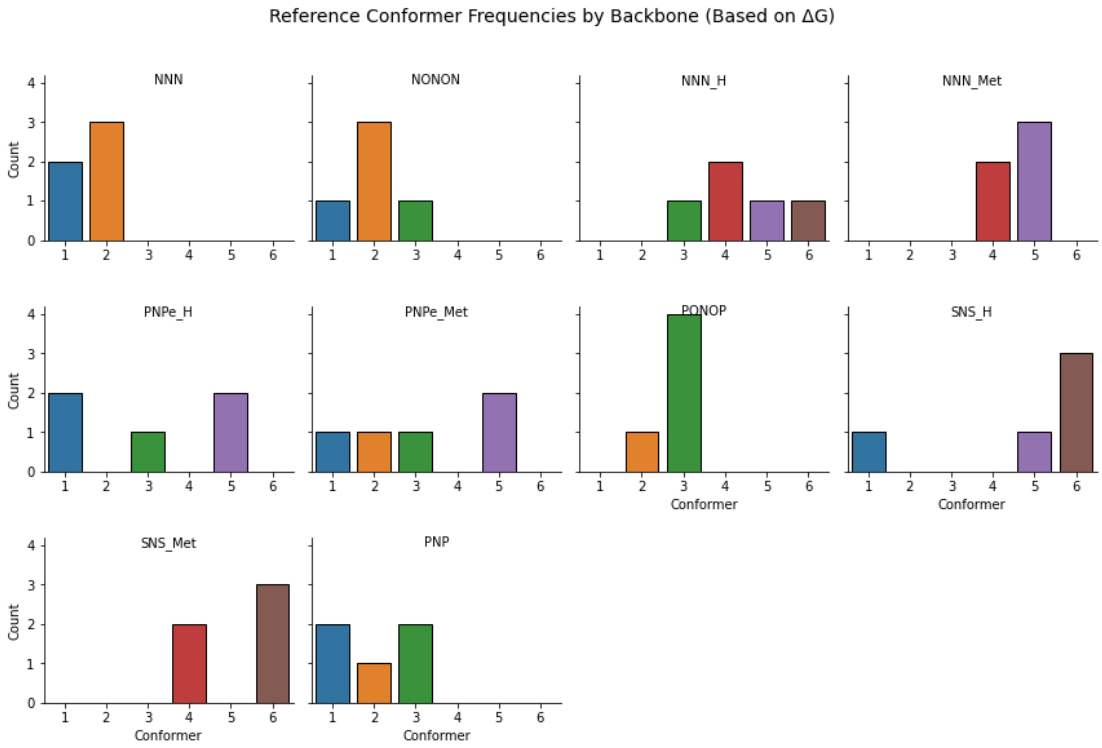

Appendix E 2: Graph depicting the frequency of most stable conformers per backbone in the pyridine complexes.

Appendix F: Declaration of AI Use

In the making of this report, I used OpenAI's ChatGPT to assist me in the making of graphs, refining language, refining word flow and clarity. Specifically:

- **Making of graphs**: I used the AI to help me code the graphs to display data from the report. For each graph I carefully looked at my data to see if all of it was correctly plotted.

- **Language Refinement**: After writing sections in the report, I used the tool to suggest improvements in sentence structure, grammar, and clarity. Each of these suggestions were carefully reviewed, only the suggestions that actively made improvements to grammar and clarity of writing were integrated.

Overview

Tool	Chapter	Use
ChatGPT-4o	All	To improve grammar, spelling, and clarity
ChatGPT Code Checker	Results and discussion	To help with making of graphs in Python

Reflection

While the use of AI is helpful for the making of graphs in Python, it is far from perfect. More times than not the code would not improve at all. I ensured at the end of the making of each graph that the actual data is what is plotted.
To ensure that all the text and ideas are my own, I only used AI to improve my writing after completing the writing of sections. All critical arguments and conclusions were developed independently. Any facts suggested by the AI were fact-checked.